chemosensors

MDPI

Article

DFT Investigation on the Adsorption and Sensing Mechanisms of Transformer Fault Gases over MOF-Based Cu-BTC and ZIF-8

Yunhua He [1], Yuhang Xie [1,*], Xin Zheng [1], Hanyu Li [1], Xianfeng Lang [2] and Yongsheng Luo [3]

[1] Electric Power Research Institute of Yunnan Power Grid Co., Ltd., Kunming 650000, China
[2] Xishuangbanna Power Grid of Yunnan Power Grid Co., Ltd., Jinghong 666100, China
[3] Dehong Power Grid of Yunnan Power Grid Co., Ltd., Mangshi 678400, China
* Correspondence: 13022355424@163.com

Abstract

Real-time detection of the six characteristic gases dissolved in transformer oil (H_2, CO, CO_2, CH_4, C_2H_4, C_2H_2), present from sub-ppm levels for C_2H_2 to several thousand ppm for CO_2, is essential for early fault diagnosis in oil-immersed power equipment, yet conventional metal-oxide sensors require elevated operating temperatures and suffer from poor selectivity. Density functional theory is used here to evaluate two metal–organic frameworks, Cu-BTC and ZIF-8, as room-temperature sensing candidates for these gases. Adsorption energy, charge transfer, DOS, work-function variation and temperature-dependent recovery time are analyzed for all twelve systems. Cu-BTC exhibits the strongest response to CO (adsorption energy: −1.745 eV, charge transfer: 0.426 e) with pronounced C-2p/Cu-3d hybridization, whereas ZIF-8 shows the strongest affinity toward C_2H_2 (adsorption energy: −1.986 eV); the two frameworks thus display complementary selectivity. Weakly bound systems desorb within microseconds to seconds at room temperature, enabling rapid regeneration, while CO on Cu-BTC and C_2H_2 on ZIF-8 are retained almost irreversibly and suit gas capture better. These results provide a theoretical basis for MOF-based on-line monitoring of dissolved gases in transformer oil and power-equipment fault diagnosis.

Keywords: transformer fault gases; DFT; Cu-BTC; ZIF-8

1. Introduction

Transformers serve as core hubs for energy conversion and transmission in power systems, undertaking critical functions of voltage transformation, power distribution and energy delivery [1]. Their safe and stable operation is directly associated with the power supply reliability and economic benefits of the entire grid [2]. However, under the coupled effects of electrical, thermal and mechanical stresses during long-term service, decomposition and even local breakdown, which generates various characteristic fault gases [3–7]. During fault development, the dissolved-gas composition evolves systematically with fault temperature and severity. H_2 and CH_4 are generated first, in small amounts, when low-temperature overheating (~150 °C) or partial discharge begins; C_2H_6 appears around 250 °C, C_2H_4 becomes dominant at 300–700 °C as thermal decomposition accelerates, and C_2H_2 forms only above ~500–700 °C, where even trace amounts indicate high-energy arcing, whereas CO and CO_2 accumulate slowly during long-term cellulose degradation. These gases dissolve in the oil over concentrations spanning several orders of magnitude: typical values for in-service transformers are H_2 50–150, CH_4 30–130, C_2H_4 60–280, C_2H_2 1–20, CO 400–900 and CO_2 3800–14,000 ppm. C_2H_2, the most diagnostic species, has the

Check for updates

Received: 9 September 2026
Revised: 3 October 2026
Accepted: 10 October 2026
Published: 13 October 2026

Copyright: © 2026 by the authors. Licensee MDPI, Basel, Switzerland. This article is an open access article distributed under the terms and conditions of the Creative Commons Attribution (CC BY) license.

lowest concentration and thus sets the most stringent detection-limit requirement, whereas CO_2 reaches several thousand ppm. A practical detector must therefore combine a low detection limit, a wide dynamic range and high selectivity, which motivates the evaluation of MOF-based materials in this work. Because the gas composition can change rapidly during fault escalation, practical online fault-gas monitoring should provide near-real-time detection; commercial DGA analyzers therefore target analysis cycles of tens of minutes to enable early warning before catastrophic failure [8–10]. Therefore, accurate detection and quantitative analysis of dissolved characteristic gases in oil enable early identification of latent defects inside transformers and evaluation of fault progression and hazard level. Accordingly, research on high-performance characteristic gas sensing technologies is highly imperative [11–13].

Traditional gas-sensitive materials are mainly represented by metal oxide semiconductors (MOS) and two-dimensional materials. Despite high sensitivity, MOS materials generally require high-temperature operation, along with severe cross-sensitivity and poor selectivity [14]. While two-dimensional materials support room-temperature detection, they commonly face challenges such as difficult recovery, baseline drift and limited selectivity [15]. Other classes explored for this application carry analogous limitations: noble-metal catalytic layers (Pt, Pd) work near room temperature with good selectivity but are prone to poisoning; carbon nanotubes respond at room temperature yet require surface modification and recover slowly and incompletely; conducting polymers are constrained by rapid aging. Above all, the technique currently used in practice, namely gas-chromatography-based dissolved-gas analysis, is accurate but off-line and periodic, and therefore cannot deliver the near-real-time monitoring required for early warning. The conventional options thus impose a compromise: heating improves recovery but costs power consumption and cross-sensitivity, whereas room-temperature operation tends to sacrifice recovery and baseline stability. MOFs escape this compromise, because room-temperature operation removes the heating requirement while the chemically tunable adsorption sites allow the binding strength, and hence both selectivity and recovery, to be adjusted through the choice of metal node and linker.

Gas sensing in MOFs stems from adsorption-induced electronic modulation. Target gases bind at high-affinity surface sites, and the interaction spans the range from physisorption to chemisorption depending on the electronic structure of the gas and of the surface site. Donor/acceptor adsorbates drive interfacial charge transfer, changing carrier concentration, Fermi level, work function, and possibly band gap, hence the conductivity or resistance underlying the response; desorption restores the baseline [16]. Specifically, Cu-BTC is built from dinuclear copper paddlewheel secondary building units coordinated with 1,3,5-benzenetricarboxylate ligands; after activation, it exposes coordinatively unsaturated Cu sites and possesses a three-dimensional interpenetrating pore structure. ZIF-8, formed by Zn^{2+} and 2-methylimidazole ligands, adopts a zeolitic sodalite topology with uniform aperture and outstanding thermal and chemical stability. These two frameworks were selected from the large MOF family precisely because the structural features described above translate into two contrasting surface chemistries. The coordinatively unsaturated Cu(II) sites of Cu-BTC (d^9) interact strongly with adsorbates carrying lone-pair or π electrons such as CO and C_2H_4, and its large specific surface area supplies a high density of such sites. ZIF-8, by contrast, contains Zn(II) with a filled d^{10} shell and presents an outer surface terminated by the methyl groups of the 2-methylimidazole linker, with no open metal sites; it therefore binds more weakly and less specifically, but is hydrophobic and thermally robust. These two materials are thus complementary: Cu-BTC provides strong, site-specific binding that favors sensitivity, whereas ZIF-8 offers weak and reversible binding that favors recovery, and the contrast between them is what makes a two-element array capable of

distinguishing the six gases. It should be noted that the present work employs slab surface models, so the response discussed here originates from surface-site chemistry rather than pore confinement; the molecular-sieving effect expected in bulk or membrane forms will be examined in future work. Both materials show promising application potential in gas sensing. For example, Ozlem Erdem Yilmaz et al. [17]. uniformly embedded Cu-BTC into a chitosan nanofiber matrix and immobilized carbon monoxide dehydrogenase, fabricating a flexible composite nanofiber sensor that achieved highly sensitive, low detection limit, fast response and highly selective detection of CO at room temperature. Naveen Kumar Arkoti et al. [18]. compounded ZIF-8 with PEI to prepare a mixed matrix membrane (MMM) filter coated on a borophene sensor, and improved the selectivity toward NO_2 by optimizing the ZIF-8 loading concentration, with gas-sensing performance tested in the concentration range of 5–25 ppm. These findings jointly demonstrate the prominent advantages of Cu-BTC and ZIF-8 in highly sensitive and selective detection of characteristic gases from both experimental and theoretical perspectives.

Against this background, this work establishes crystal structure models of two representative MOFs, Cu-BTC and ZIF-8, in Materials Studio based on DFT, and systematically investigates their adsorption behaviors toward six fault gases in transformer oil. By calculating and analyzing key parameters including adsorption energy, charge transfer, DOS, work function variation and temperature-dependent recovery time for each adsorption system, the microscopic interaction mechanism between gas molecules and the framework is uncovered at the electronic structure level. This study is expected to provide theoretical basis and data support for the development of novel MOF-based gas sensors for on-line monitoring of dissolved gases in transformer oil, and deliver a comprehensive evaluation of the application potential of Cu-BTC and ZIF-8 in power equipment fault diagnosis.

2. Computational Detail

All first-principles calculations in this work were performed using the DMol3 module embedded in Materials Studio 2020, which is built upon the density functional theory (DFT) framework with a localized atomic orbital basis set approach [19]. The exchange-correlation energy of electrons was described by the Perdew–Burke–Ernzerhof (PBE) functional under the generalized gradient approximation (GGA) [20–22]. Core electrons of all atoms were treated with norm-conserving pseudopotentials, while valence electrons were expanded with the double numerical plus polarization (DNP) basis set [23,24]. Grimme's DFT-D2 empirical dispersion correction was incorporated into all calculations [25,26]. Self-consistent field energy convergence precision set to 5.0×10^{-5} Ha [27,28].

For model construction, two classic metal–organic framework materials, Cu-BTC and ZIF-8, were employed as adsorption substrates. Surface models and initial adsorption configurations. Periodic slab models of Cu-BTC and ZIF-8 were constructed by cleaving the optimized bulk structures along the (001) plane. The (001) facet was selected for both materials because it is a low-index, closely packed and thermodynamically stable surface that is predominantly exposed on the experimentally observed cubic (Cu-BTC) and truncated-rhombic-dodecahedral (ZIF-8) crystallites; moreover, it presents the characteristic pore apertures (the square channels of Cu-BTC and the six-membered-ring windows of ZIF-8) through which gas molecules approach the framework. For Cu-BTC, the gas molecule was initially placed at the geometric center of the exposed square pore, equidistant from the surrounding Cu paddle-wheel units and organic linkers. This symmetric, unbiased configuration avoids pre-assigning the molecule to any specific site (e.g., an open Cu site or a window site), allowing it to migrate freely during full geometry relaxation and to settle at the energetically most favorable adsorption site. For ZIF-8, the outermost layer of the (001) surface consists exclusively of hydrogen atoms of the methyl groups of the

2-methylimidazolate linkers, and these surface H atoms are chemically equivalent owing to the surface symmetry and the free rotation of the methyl groups. Consequently, the molecule was initially positioned above an arbitrary surface H atom, which is representative of all equivalent outer-surface adsorption locations. A 20 Å-thick vacuum slab was added perpendicular to the material surface to eliminate periodic interactions between adjacent layers and ensure the reliability of calculation results [29]. Considering the large lateral size of the constructed MOF surface systems, a $5 \times 5 \times 1$ Gamma-centered k-point mesh was applied for both structure optimization and electronic property calculations. These parameter configurations have been extensively validated to guarantee the physical validity of calculation results for porous crystalline materials.

$$E_{ads} = E_{gas/materials} - E_{gas} - E_{materials} \quad (1)$$

The adsorption energy is defined by Equation (1), which corresponds to the total energy change of the system upon gas adsorption. Specifically, it is calculated as the difference among the total energy of the gas-adsorbed MOF system, the energy of the bare MOF substrate, and the energy of an isolated gas molecule in vacuum [30].

$$Q_T = Q_{\text{after}} - Q_{\text{before}} \quad (2)$$

Equation (2) defines the charge transfer amount (Q). This parameter quantifies the strength of electronic coupling between gas molecules and the MOF skeleton by measuring the charge variation of gas molecules before and after the adsorption process [31,32].

$$\tau = A^{-1}\mathrm{e}^{-\frac{E_{\text{ads}}}{K_B T}} \quad (3)$$

The desorption time (τ) is derived from Equation (3) based on the correlation between adsorption energy and ambient temperature. As a critical index to evaluate the recyclability of gas sensing materials, this parameter reflects the time required for adsorbed gas molecules to detach from the substrate surface at a given temperature [33,34].

3. Results and Discussions

3.1. Structural Optimization

Figure 1 displays ball-and-stick models and key structural parameters of six representative small molecules after geometric optimization, which intuitively demonstrate the regulatory effects of bond order and atomic hybridization modes on molecular spatial configurations.

Both H_2 are linear diatomic molecules. The H–H single bond has a length of 0.749 Å, while the C–O triple bond measures 1.143 Å, corresponding to the typical bonding features of nonpolar and polar covalent bonds, respectively. CO_2 is a highly symmetric linear triatomic molecule with an sp-hybridized central carbon atom. The C=O double bond length is 1.177 Å, and the O–C–O bond angle reaches 179.986°, which is nearly consistent with the ideal linear geometry. CH_4 possesses a standard tetrahedral structure. The central carbon atom forms four equivalent C–H bonds via sp^3 hybridization, with a bond length of 1.100 Å and an H–C–H bond angle of 109.488°, which matches well with the theoretical tetrahedral bond angle. As a linear alkyne molecule, C_2H_2 features a C≡C triple bond constructed by sp-hybridized carbon atoms. The triple bond length is 1.208 Å and the C–H bond length is 1.072 Å, with all atoms arranged collinearly. C_2H_4 is a planar alkene molecule with sp^2-hybridized carbon atoms. The C=C double bond length is 1.334 Å and the C–H bond length is 1.094 Å. The H–C–H and H–C=C bond angles are 116.488° and 121.703°, respectively, and all atoms within the molecule lie on the same plane.

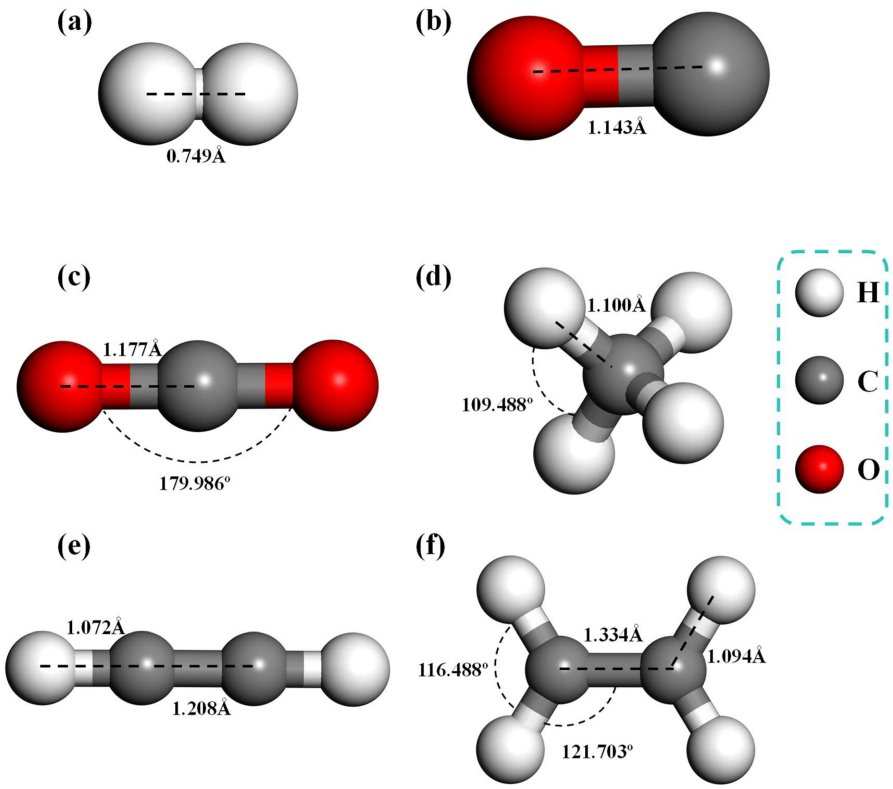


Figure 1. Optimized models of gas molecules: (**a**) H_2, (**b**) CO, (**c**) CO_2, (**d**) CH_4, (**e**) C_2H_2, (**f**) C_2H_4.

ZIF-8 is a representative zeolitic imidazolate framework assembled via coordination interactions between metal ions and 2-methylimidazole ligands (Figure 2a,c). From the top view, uniform pore windows surrounded by imidazole ligands are clearly distinguishable, forming a well-ordered channel system with sodalite (sod) topology. The side view distinctly manifests the axial extension of its three-dimensional skeleton, featuring highly ordered porosity and strong framework rigidity.

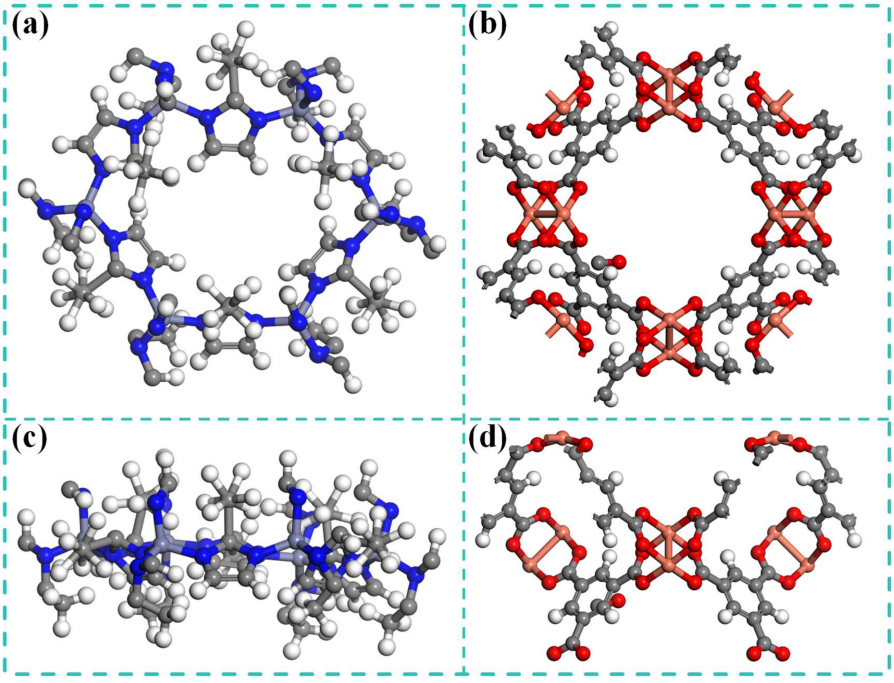


Figure 2. Optimized material: top views of (**a**) ZIF-8 and (**b**) Cu-BTC; side views of (**c**) ZIF-8 and (**d**) Cu-BTC.

Cu-BTC is constructed with dinuclear copper paddlewheel units as metal nodes, which are linked by 1,3,5-benzenetricarboxylate ligands through carboxylate coordination (Figure 2b,d). Its top view exhibits a periodically arranged array of three-dimensional pore cages, whereas the side view reflects the layered expansion pattern of the framework along the vertical direction. With hierarchical pore channels and exposed open metal sites, Cu-BTC demonstrates prominent structural stability and considerable potential for functional modification.

3.2. The Adsorption of Gas on Materials

Prior to the detailed discussion, it is necessary to clarify the surface interactions involved in the sensing mechanism. Gas sensing on Cu-BTC and ZIF-8 proceeds through reversible adsorption rather than chemical conversion: no bond cleavage or new species formation was observed in any optimized structure. On Cu-BTC, CO chemisorbs at the coordinatively unsaturated Cu sites through coordination bonding, involving electron donation from the CO lone pair to Cu and back-donation from Cu 3d orbitals to the antibonding orbital of CO, consistent with the strong C-2p/Cu-3d hybridization and large charge transfer (0.426 e). C_2H_4 binds to the same sites through pi-complexation with moderate strength. In contrast, ZIF-8 has no open metal sites, and its strong adsorption of C_2H_2 (-1.986 eV) is attributed to C-H···N hydrogen bonding between the acetylenic hydrogen and the nitrogen atoms of the imidazolate linkers, reinforced by pi-interactions with the linker framework, while the weakly adsorbed gases are dominated by van der Waals physisorption. The interfacial charge transfer associated with these interactions modulates the carrier concentration and work function of the framework, generating the electrical sensing signal, and desorption reverses this process to restore the baseline.

Figure 3 depicts the optimized adsorption geometries and corresponding, on the Cu-BTC framework. The generally short separation distances suggest relatively intense interactions between the gas molecules and framework skeleton. CO yields the most negative adsorption energy of -1.745 eV on Cu-BTC. This finding indicates that pronounced electron redistribution takes place between CO and the unsaturated Cu sites, giving rise to strong chemisorption and enabling Cu-BTC to deliver optimal adsorption strength toward CO. C_2H_4 ranks second in interaction strength. CO_2, H_2 and CH_4 fall into the category of moderate physisorption. By contrast, C_2H_2 exhibits the weakest adsorption behavior with merely -0.163 eV in adsorption energy and 0.042 e in charge transfer. Overall, Cu-BTC shows the most remarkable adsorption selectivity for CO.

Relative to Cu-BTC, all gas species on ZIF-8 show markedly larger adsorption distances, falling within the range of 3.172–4.301 Å (Figure 4). Specifically, H_2 has the shortest adsorption distance (3.172 Å) and C_2H_4 longest (4.301 Å), suggesting that weak physisorption dominates the interaction between ZIF-8 skeleton and most gas.

The E_{ads} of C_2H_2 on ZIF-8 reaches -1.986 eV, with an absolute value far greater than those of other gas systems, indicating an abnormally intense adsorption behavior (Table 1). Even with a low charge transfer of 0.142 e and an adsorption distance of 3.152 Å, this finding implies the presence of specific strong interactions between C_2H_2 and the ZIF-8 framework. C_2H_4 and CH_4 feature relatively strong adsorption, with adsorption energies of -1.062 eV and -0.871 eV and charge transfers of 0.298 e and 0.260 e, respectively. By comparison, CO, CO_2 and H_2 exhibit weaker interactions.

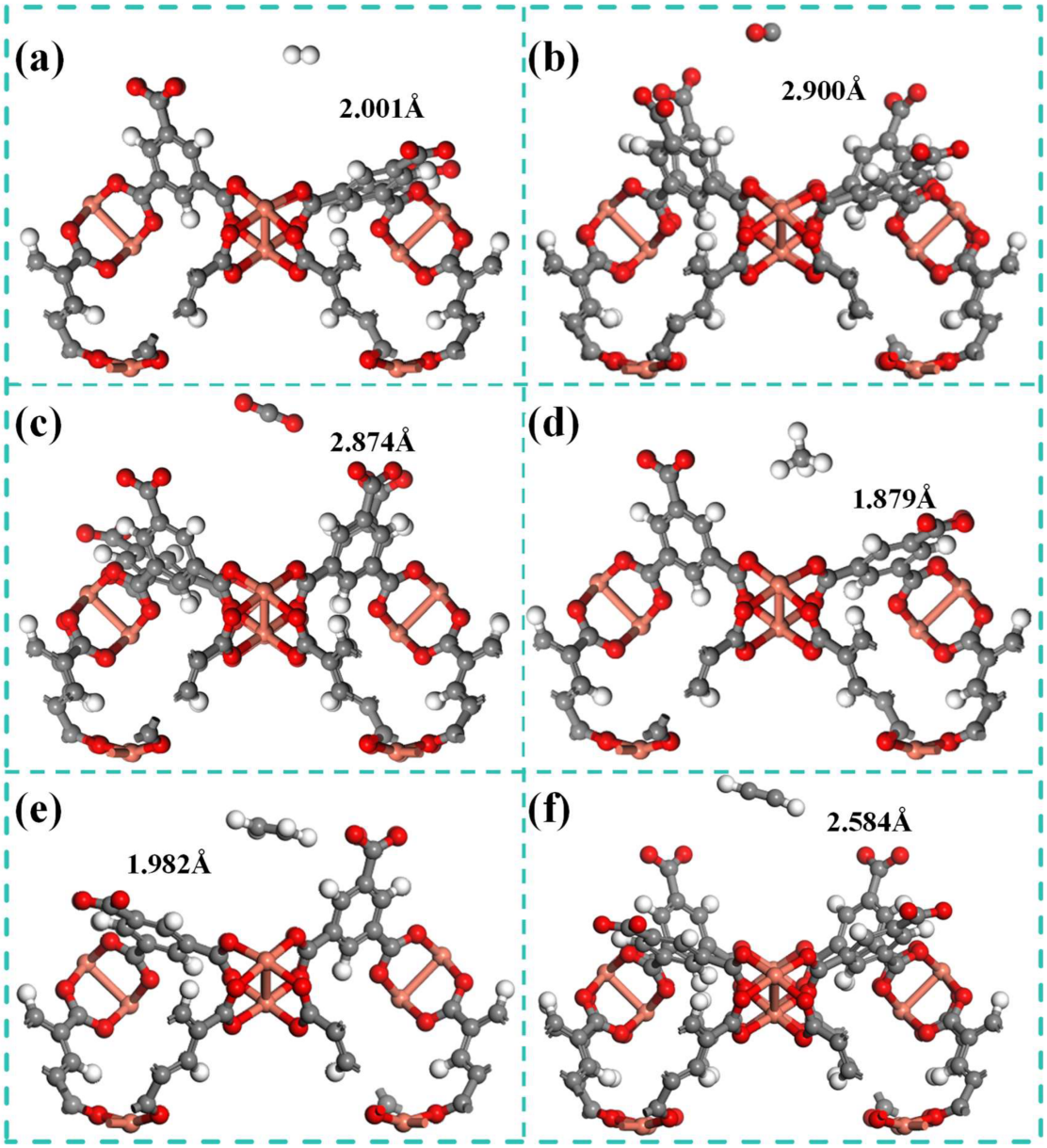


Figure 3. Gas adsorption models on Cu-BTC: (**a**) H_2, (**b**) CO, (**c**) CO_2, (**d**) CH_4, (**e**) C_2H_4, (**f**) C_2H_2.

Table 1. Gas adsorption parameters.

Material	Gas	E_{ads} (eV)	Q_T (e)	D (Å)	E_g
Cu-BTC	H_2	−0.544	0.003	2.001	1.936
	CO	−1.745	0.426	2.900	2.127
	CO_2	−0.599	0.223	2.874	1.773
	CH_4	−0.541	0.260	1.874	1.909
	C_2H_4	−0.815	0.254	1.982	2.072
	C_2H_2	−0.163	0.042	2.584	1.935
ZIF-8	H_2	−0.272	0.003	3.172	3.959
	CO	−0.506	0.125	3.506	3.933
	CO_2	−0.397	0.223	3.955	3.795
	CH_4	−0.871	0.260	3.716	3.823
	C_2H_4	−1.061	0.298	3.790	3.443
	C_2H_2	−1.986	0.142	3.152	3.823

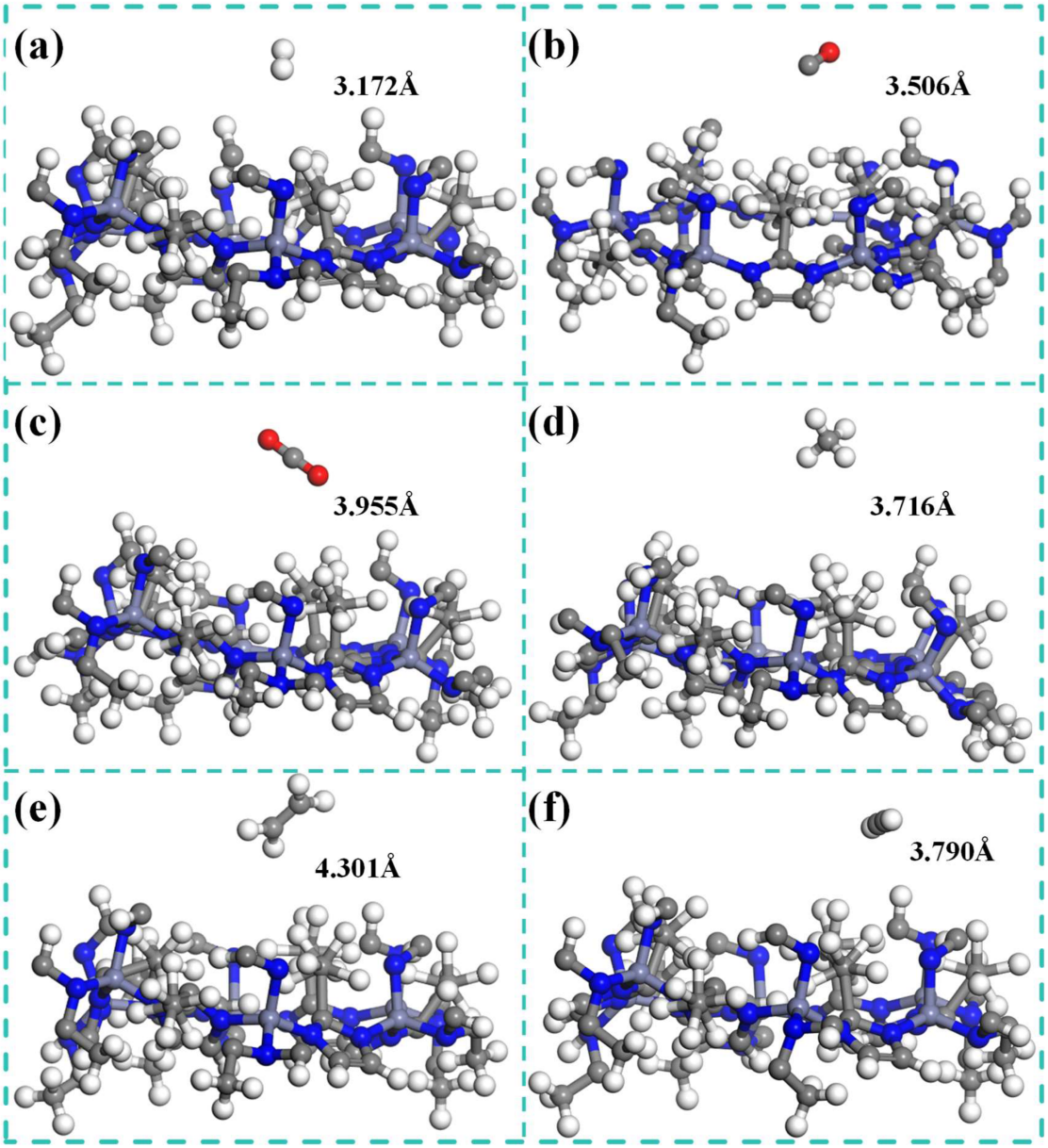


Figure 4. Gas adsorption models on ZIF-8: (**a**) H_2, (**b**) CO, (**c**) CO_2, (**d**) CH_4, (**e**) C_2H_4, (**f**) C_2H_2.

CO stands out as the most strongly adsorbed species, featuring the most negative adsorption energy (−1.745 eV) and the largest charge transfer (0.426 e), while C_2H_2 yields the weakest response with the smallest adsorption energy magnitude (−0.163 eV). For ZIF-8, C_2H_2 delivers exceptionally strong specific adsorption, significantly outperforming other gases, whereas H_2 expresses the weakest adsorption. Cu-BTC has better adsorption capacity for CO, CO_2 and H_2 than ZIF-8, whereas ZIF-8 exhibits stronger adsorption affinity toward C_2H_2, C_2H_4 and CH_4. The charge transfer trends of both materials are largely consistent with their adsorption energy profiles, jointly confirming their complementary gas selectivity. Systematic trends with gas chemistry and framework surface chemistry. The adsorption parameters vary systematically with the electronic structure of the gases. The saturated, nonpolar gases (H_2, CH_4 and C_2H_6) interact the weakest: H_2 exhibits the smallest charge transfer (Q_T = 0.003 e) and among the least negative adsorption energies on both frameworks (−0.544 and −0.272 eV), and the separately evaluated C_2H_6 is even more weakly bound (E_{ads} = −0.058 eV), consistent with their low polarizability and their lack of a permanent dipole, quadrupole, lone-pair or π electrons, i.e., essentially dispersion-

driven physisorption that gives little electronic response. The unsaturated hydrocarbons interact through their π clouds: C_2H_4 binds appreciably on both Cu-BTC and ZIF-8 (−0.815 and −1.061 eV) with substantial charge transfer (0.254 and 0.298 e) and short distances, reflecting donor–acceptor coupling of the C=C electrons with the framework, whereas C_2H_2 adsorbs only weakly on Cu-BTC (−0.163 eV, Q_T = 0.042 e) but shows a framework-specific, exceptionally strong interaction on ZIF-8 (−1.986 eV), the origin of which is analyzed from its optimized geometry in Figure 4f and Section 3.2. The polar gases are most sensitive to open metal sites: CO gives the strongest adsorption and largest charge transfer on Cu-BTC (−1.745 eV, 0.426 e), attributable to coordination of its carbon-end lone pair to the coordinatively unsaturated Cu sites, whereas it is much weaker on the H-terminated ZIF-8 (−0.506 eV, 0.125 e); CO_2 shows intermediate, quadrupole-driven binding (−0.599 and −0.397 eV). Overall, gases with lone-pair or π electrons (CO, C_2H_4) respond most strongly to the open-Cu surface, while nonpolar saturated gases show weak, reversible physisorption; the uniformly longer adsorption distances on ZIF-8 (3.17–4.30 Å) than on Cu-BTC (1.87–2.90 Å) further distinguish short-range chemical coordination on Cu-BTC from weaker outer-surface adsorption on ZIF-8.

3.3. Dos and Tdos Analysis

Figure 5a corresponds to the CO/Cu-BTC system, where the TDOS undergoes pronounced reconstruction in the vicinity of the Fermi level upon gas adsorption, accompanied by a substantial emergence of new electronic states (Figure 5). The PDOS reveals extensive overlap between the C-2p and O-2p orbitals of the CO molecule and the Cu-3d orbitals of the Cu-BTC framework across the energy range of −8 to 0 eV. This observation signifies robust orbital hybridization and chemisorption between CO and the coordinatively unsaturated Cu sites.

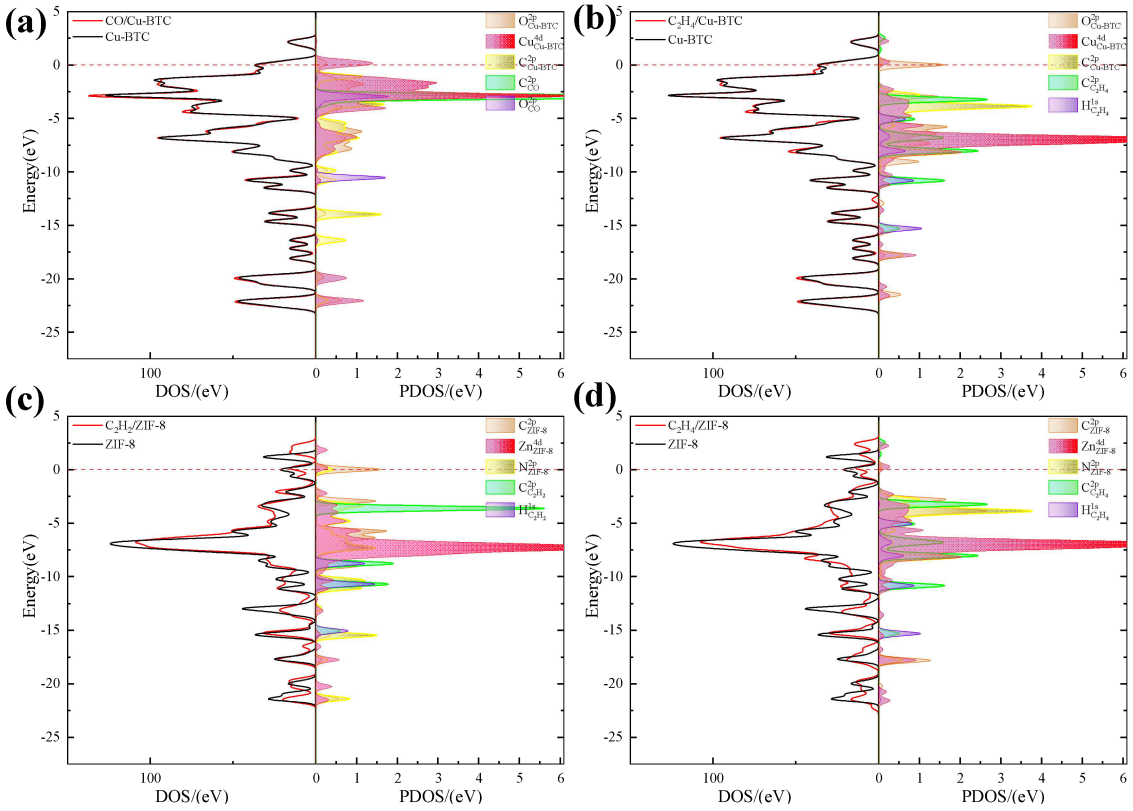


Figure 5. Density of states for typical gas adsorption systems: (**a**) CO/Cu-BTC, (**b**) C_2H_4/Cu-BTC, (**c**) C_2H_2/ZIF-8, (**d**) C_2H_4/ZIF-8.

Figure 5b illustrates the C_2H_4/Cu-BTC system, where a moderate increase in TDOS near the Fermi level is discernible after adsorption. The C-2p orbitals of C_2H_4 overlap with the Cu-3d orbitals within −6 to 0 eV; nevertheless, the hybridization intensity is markedly attenuated relative to the CO/Cu-BTC system. Contributions from H-1s orbitals are predominantly localized in the deep energy region, suggesting that the interaction between C_2H_4 and Cu sites falls into the moderate chemisorption regime.

Figure 5c depicts the C_2H_2/ZIF-8 system, where the TDOS near the Fermi level is dramatically augmented with newly emerged peaks following adsorption. These findings corroborate the exceptionally strong and selective adsorption of C_2H_2 on ZIF-8 (−1.986 eV) from an electronic structure perspective.

Figure 5d shows the C_2H_4/ZIF-8 system, where a certain degree of overlap between C-2p and N-2p orbitals can be identified; however, both the intensity and distribution range of hybridization peaks are inferior to those of the C_2H_2/ZIF-8 system, indicating weaker electronic state coupling that corresponds to its lower adsorption energy (−1.061 eV).

3.4. Work Function Analysis

In the Cu-BTC system depicted in Figure 6a, the pristine sample shows the lowest work function value, which rises at varying levels after gas adsorption. Specifically, CO_2 adsorption triggers the most pronounced increase, pushing the work function to a peak of 7.32 eV. Moderate work function increments are observed for CO, CH_4 and C_2H_4, whereas CO gives rise to the weakest response, highlighting the distinct gas selectivity of Cu-BTC.

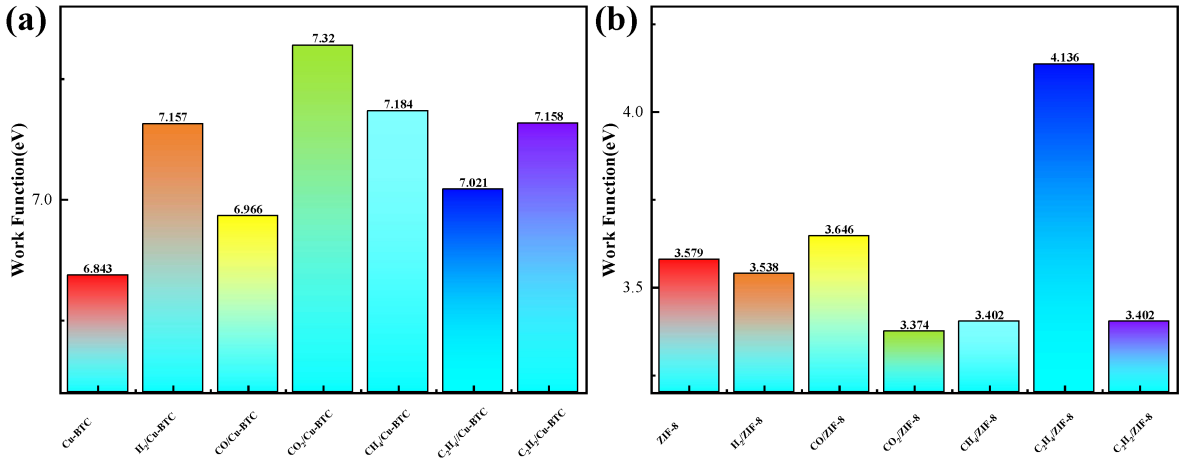


Figure 6. Comparison of work functions: (**a**) Cu-BTC, (**b**) ZIF-8.

For the ZIF-8 system in Figure 6b. A sharp rise in work function to 4.136 eV occurs exclusively upon C_2H_4 adsorption, which is much higher than those of other gas systems and verifies its specific recognition capability for C_2H_4. The differentiated response patterns of the two materials lay a theoretical foundation for their practical applications in selective gas sensing.

3.5. Recovery Time Analysis

Figure 7 presents the comparison of recovery times for six gasses on ZIF-8 and Cu-BTC across three temperatures. In the ZIF-8 system, C_2H_2 consistently shows much longer recovery times than the other gas molecules at all tested temperatures, and cannot be effectively recovered even at the highest temperature, with values of 2.34×10^{32} s at 498 K, matching its strongest adsorption energy (−1.986 eV) and exceptionally long recovery time. C_2H_4 and CH_4 follow in sequence: the recovery time of C_2H_4 decreases to 27.47 s at 398 K and becomes even shorter at 498 K, whereas CH_4 exhibits a recovery time of 533 s at room

temperature (298 K) and desorbs progressively faster as the temperature rises. By contrast, CO, CO_2 and H_2 are only weakly adsorbed and thus cannot be effectively adsorbed on ZIF-8, exhibiting negligible, ultrashort recovery times at 498 K, indicative of essentially spontaneous desorption behavior.

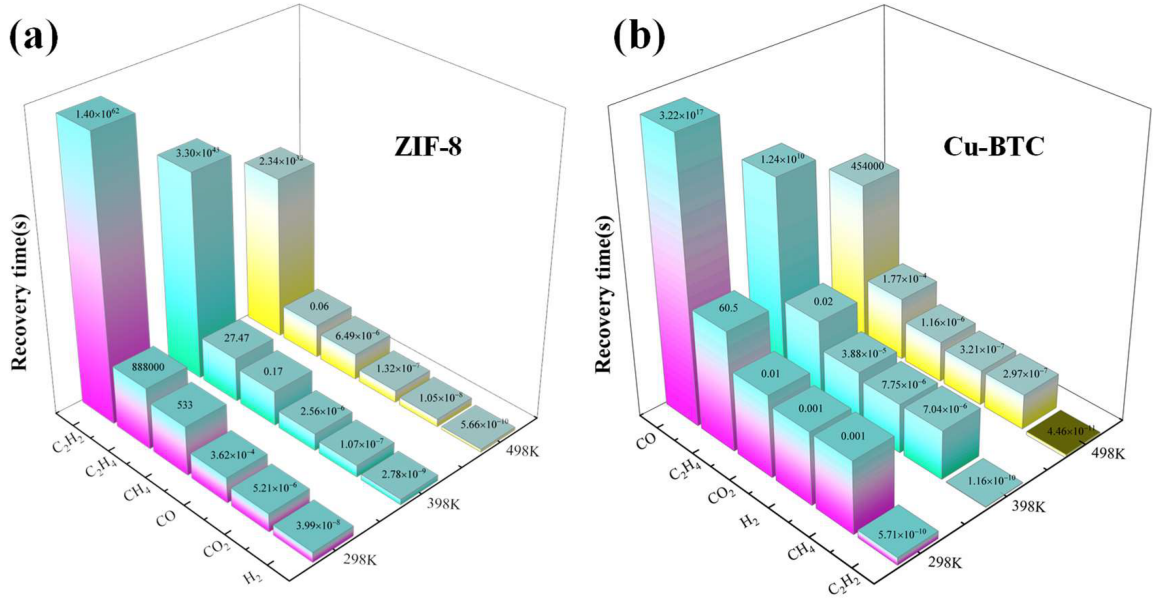


Figure 7. Analysis of recovery times: (**a**) ZIF-8, (**b**) Cu-BTC.

For the Cu-BTC system, CO possesses the longest recovery time, reaching 3.22×10^{17} s at 498 K and showing virtually no recovery even at such a high temperature, while C_2H_4 exhibits a recovery time of 60.5 s at 298 K that is further shortened upon heating. The remaining gases, including C_2H_2, are too weakly adsorbed to be effectively retained on Cu-BTC, in line with their weak adsorption energies and minimum Qt. Furthermore, both materials yield extremely short recovery times for these weakly adsorbed gases even at room temperature, which precludes effective gas retention while facilitating the fast cyclic regeneration of gas sensors. The ultra-long recovery times of C_2H_2 on ZIF-8 and CO on Cu-BTC—remaining virtually unrecoverable even at 498 K—show nearly irreversible adsorption features, rendering them more applicable for gas capture and sequestration scenarios.

3.6. Temperature-Dependent Sensing Response and Selectivity

To quantitatively evaluate the sensing response of the two frameworks, the conductivity change induced by adsorption is assessed. In general, the conductivity σ depends strongly on the band gap E_g and can be approximated by Equation (4):

$$\sigma \propto \exp\left(-E_g/2k_BT\right) \tag{4}$$

Sensitivity (S) is an essential metric for evaluating sensor performance and is defined here through the conductance change, $S = \sigma_{gas/MOF}/\sigma_{MOF} - 1$, which follows from Equation (4) as Equation (5):

$$S = \exp\left[\frac{E_{g_{MOF}} - E_{g_{gas\ /MOF}}}{2K_BT}\right] - 1 \tag{5}$$

The pristine band gaps are taken as 2.25 eV for Cu-BTC and 4.00 eV for ZIF-8. The resulting sensitivities are compared in Figure 8.

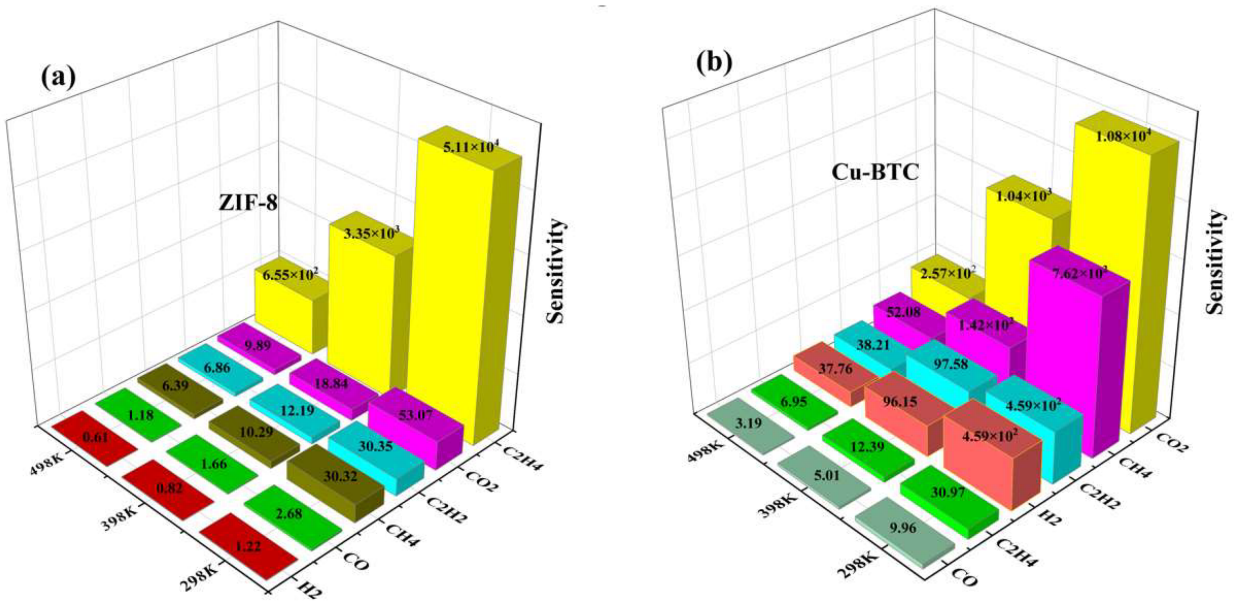


Figure 8. Analysis of sensitivity: (**a**) ZIF-8, (**b**) Cu-BTC.

Figure 8b compares the sensitivities of Cu-BTC toward the six gases at 298 K. Cu-BTC exhibits the highest sensitivity to CO_2 (1.08×10^4), exceeding those toward CH_4, C_2H_2 and H_2 by a factor of 14–24 and those toward C_2H_4 (31.0) and CO (9.96) by two to three orders of magnitude; CO gives the lowest value. The overall order follows $CO_2 > CH_4 > C_2H_2 > H_2 > C_2H_4 > CO$, demonstrating that Cu-BTC can effectively discriminate among the six fault gases. CO, which has the largest $|E_{ads}|$ on Cu-BTC (1.745 eV), combines the weakest response with a prohibitively long recovery time, whereas CO_2, adsorbed much more weakly (0.599 eV), offers both the highest sensitivity and a much shorter recovery time and is therefore the preferred sensing target on this framework.

Figure 8a presents the corresponding results for ZIF-8. The highest sensitivity is obtained for C_2H_4 (5.11×10^4), exceeding those of the other five gases by two to four orders of magnitude, whereas H_2 gives the lowest value (1.22); the order follows $C_2H_4 > CO_2 > CH_4 \approx C_2H_2 > CO > H_2$. It should be noted that C_2H_2, despite having the largest $|E_{ads}|$ on ZIF-8 (1.986 eV), shows only a moderate response (30.4) and desorbs almost irreversibly, so ZIF-8 is better suited to sensing C_2H_4 and to the strong capture of C_2H_2. Comparison of the two panels further shows that the frameworks rank the gases differently: CO_2, the strongest respondent on Cu-BTC, is only moderate on ZIF-8, whereas C_2H_4, the strongest on ZIF-8, is among the weakest on Cu-BTC. A two-element array therefore generates a distinct pair of responses for each gas rather than a single common ordering, which is the basis for pattern-recognition-based identification of the six gases.

The influence of temperature is illustrated by the same figure. Since ΔE_g is fixed while K_BT increases, S decreases monotonically with temperature for every system: the sensitivity of Cu-BTC toward CO_2 falls from 1.08×10^4 at 298 K to 1.04×10^3 at 398 K and 2.57×10^2 at 498 K, a reduction by a factor of about 42, and that of ZIF-8 toward C_2H_4 falls from 5.11×10^4 to 3.35×10^3 and 6.56×10^2, a reduction by about 78. Raising the temperature thus weakens the response but shortens the recovery time, so the operating point must satisfy two opposing requirements simultaneously, namely, $S \geq 1$ for a detectable signal and a recovery time compatible with the monitoring cycle. On this basis, 298–398 K is identified as the usable window, since at 398 K every system still gives $S > 1$ except H_2 on ZIF-8 (0.82), whereas heating to 498 K costs one to two orders of magnitude in response. It is further noted that the common environmental molecules N_2, O_2 and H_2O adsorb on both frameworks with absolute adsorption energies below 0.2 eV and negligible charge

transfer, i.e., in the weak physisorption regime, and are therefore not expected to interfere significantly with the detection of the six fault gases (Table 2). In practical analysis, the six fault gases coexist, and competitive adsorption must be considered: on Cu-BTC the strongly bound CO preferentially occupies the open Cu sites and may suppress the uptake of weakly bound coexisting gases, whereas, on ZIF-8, competition is expected to be milder, except for the strongly bound C_2H_2. Since the net charge transfer and work-function change are dominated by the strongly adsorbed component, mixture analysis relies on the distinct response pairs of the dual-element array rather than on single-element selectivity; explicit co-adsorption calculations at finite coverages are left for future work.

Table 2. Adsorption energy and charge transfer of N_2, O_2 and H_2O on Cu-BTC and ZIF-8.

Material	Environmental Small Molecules	E_{ads} (eV)	Q_T (e)
Cu-BTC	N_2	−0.152	0.002
	O_2	−0.134	0.005
	H_2O	−0.131	0.003
ZIF-8	N_2	−0.098	0.005
	O_2	−0.109	0.008
	H_2O	−0.112	0.003

4. Conclusions

The adsorption performance property of two representative metal–organic framework (MOF) materials, Cu-BTC and ZIF-8. The results clearly demonstrate the distinct advantages of the two materials in gas recognition and capture.

(1) Cu-BTC exhibits the strongest adsorption affinity towards CO, with an adsorption energy of −1.745 eV, endowing it with optimal selective recognition capability for CO. ZIF-8 shows extremely strong specific adsorption to C_2H_2, with an adsorption energy as high as −1.986 eV. Its adsorption strength far exceeds that of the other five gases, making C_2H_2 the most favorable adsorption target in this system. The gas adsorption preferences of the two materials present obvious complementarity, enabling differentiated responses to different target gases.

(2) The work function of ZIF-8 rises to 4.136 eV after C_2H_4 adsorption, corresponding to the largest electrical response amplitude. For Cu-BTC, the work function increases to 7.32 eV upon CO_2 adsorption, showing prominent response performance. In terms of recovery characteristics, the recovery time of ZIF-8 for C_2H_2 reaches 2.34×10^{32} s at 498 K, while that of Cu-BTC for CO reaches 3.22×10^{17} s at 498 K; desorption is barely achievable even at 498 K, indicating their suitability for C_2H_2 and CO adsorption and capture, respectively. Weak adsorption systems such as H_2 and CO_2 have recovery times as short as 10^{-8} to 10^{-20} s at room temperature, which possess great application potential for fast cyclic sensing.

(3) The high selectivity and moderate interaction strength of Cu-BTC for CO make it applicable to highly sensitive sensing and detection of CO gas. The ultra-strong adsorption capacity of ZIF-8 towards C_2H_2 can be utilized for the enrichment and separation of trace C_2H_2 in transformer oil.

(4) Based on the complementary selectivity of the two frameworks, a dual-element chemiresistive sensor array can be envisioned, in which Cu-BTC and ZIF-8 films are deposited on interdigitated electrodes and each gas produces a distinct response pattern across the two channels. Weakly adsorbed gases with microsecond-to-second desorption enable fast, reversible sensing at room temperature, whereas the nearly irreversible adsorption of CO on Cu-BTC and C_2H_2 on ZIF-8 suits the enrichment of trace fault gases, with thermal regeneration if needed. The room-temperature operation eliminates heating elements and

allows integration into online dissolved-gas monitoring devices. It should be noted that practical devices still require experimental validation under realistic atmospheres, which is the direction of our future work.

Author Contributions: Conceptualization, Y.H. and Y.X.; methodology, Y.H.; software, X.Z.; validation, Y.H., Y.X. and X.Z.; formal analysis, Y.H.; investigation, Y.H.; resources, Y.H.; data curation, Y.H.; writing—original draft preparation, Y.H.; writing—review and editing, Y.X.; visualization, Y.L.; supervision, H.L.; project administration, X.L. All authors have read and agreed to the published version of the manuscript.

Funding: This research received no external funding.

Institutional Review Board Statement: Not applicable.

Informed Consent Statement: Not applicable.

Data Availability Statement: Data will be made available on request

Conflicts of Interest: All authors were employed by the company Yunnan Power Grid Co., Ltd.

References

1. An, Q.; Li, J.; Peng, J.; Hu, L. Dissolved Gas Analysis in Transformer Oil Using Pd, Pt Doped ZnO: A DFT Study. *Chem. Phys. Lett.* **2025**, *868*, 142018. [CrossRef]
2. Li, L.; Huang, Z.; Xu, H.; Zeng, W.; Zhou, Q. Selective Detection of Dissolved Fault Gases in On-Load Tap Changer Insulating Oil Using WO_3−-Modified Janus HfSeTe: A First-Principles Study. *Surf. Interfaces* **2026**, *84*, 108662. [CrossRef]
3. Wang, Z.; Zhang, D.; Tang, M.; Chen, Q.; Zhang, H.; Shao, X. Construction of Ultra-Fast Hydrogen Sensor for Dissolved Gas Detection in Oil-Immersed Transformers Based on Titanium Dioxide Quantum Dots Modified Tin Dioxide Nanosheets. *Sens. Actuators B Chem.* **2023**, *393*, 134141. [CrossRef]
4. Huang, L.; Jiang, J.; Huang, Z.; Lu, D.; Zeng, W.; Zhou, Q. First-Principles Study of Oxygen-Rich W_3-Doped TiS_2 Monolayers for Selective Detection of CO_2 at Low Temperature. *Mater. Today Chem.* **2025**, *43*, 102484. [CrossRef]
5. Liu, Y.; Zhou, Q.; Hou, W.; Li, J.; Zeng, W. Adsorption Properties of Cr Modified GaN Monolayer for H_2, CO, C_2H_2 and C_2H_4. *Chem. Phys.* **2021**, *550*, 111304. [CrossRef]
6. Zhang, Y.; Feng, W.; Zhang, J.; Lu, D.; Zeng, W.; Zhou, Q. Enhancement of Adsorption Performance of Gases in Oil on a Cr_3-Modified SnS_2 Monolayer Based on the First Principles. *Langmuir* **2023**, *39*, 14422–14432. [CrossRef] [PubMed]
7. Teng, Z.; Lv, C.; Zhou, Q. Analysis of the Sensing Performance of Ag-Doped $Ti_3C_2O_2$ MXene for Characteristic Gases in Transformer Oil. *Chem. Phys.* **2025**, *596*, 112735. [CrossRef]
8. Palosuo, T.; Heikkinen, J.; Hilasvuori, E.; Kulmala, L.; Launiainen, S.; Lehtilä, A.; Leinonen, I.; Liimatainen, M.; Salminen, M.; Shurpali, N.; et al. Demands and Possibilities for Field-Scale Estimation of Agricultural Greenhouse Gas Balances. *CATENA* **2025**, *249*, 108649. [CrossRef]
9. Thomas, T.; Ramos Ramón, J.A.; Agarwal, V.; Méndez, A.Á.; Martinez, J.A.A.; Kumar, Y.; Sanal, K.C. Highly Stable, Fast Responsive Mo_2CT_x MXene Sensors for Room Temperature Carbon Dioxide Detection. *Microporous Mesoporous Mater.* **2022**, *336*, 111872. [CrossRef]
10. Jiang, T.; Wu, F.; Wu, H.; Xie, H.; Deng, B.; Bi, M. Adsorption and Gas Sensing Properties of CH_4, C_2H_2, and C_2H_4 Dissolved Gases in Transformer Oil on Pd_n(n = 1–4)-Doped WTe_2 Monolayers: A DFT Study. *Comput. Theor. Chem.* **2024**, *1241*, 114895. [CrossRef]
11. Li, F.; Chen, F.; Cui, H.; Jiang, X. Pristine and Ni-Doped WTe_2 Monolayer for Adsorption and Sensing of C_2H_2 and C_2H_4 in Oil-Immersed Transformers: A DFT Study. *Comput. Theor. Chem.* **2023**, *1226*, 114187. [CrossRef]
12. Li, S.; Zhu, R.; Li, Y.; Shi, S.; Li, J.; Zhang, K. Lanthanide Schiff-Base Paper-Based Composites as Fluorescence-Based Gas Sensors for Selective, Quantitative and Visual Detection of H_2S Gas. *Sens. Actuators B Chem.* **2026**, *448*, 139039. [CrossRef]
13. Tan, S.; Bi, M.; Lei, S.; He, X.; Hu, X.; He, J.; Jiang, T. Adsorption of SF_6 Decomposition Gases (H_2S, SO_2 and SOF_2) on TM (Pd and Pt) Modified Monolayer ZrS_2: A DFT Study. *Comput. Theor. Chem.* **2024**, *1236*, 114586. [CrossRef]
14. Qi, S.; Dai, L.; Meng, W.; Li, Y.; Wang, L. Amperometric Type NO_2 Sensor Based on $La_{0.75}Sr_{0.25}Cr_{0.5}Fe_{0.5}O_3$-δ-$Bi_2O_3$ Sensing Electrode Prepared by Self-Demixing. *Sens. Actuators B Chem.* **2023**, *378*, 133136. [CrossRef]
15. Xu, H.; Li, L.; Xia, J.; Zeng, W.; Zhou, Q. Innovative Doping Strategies in $ZrSe_2$: Co and Rh for Enhanced Agricultural Greenhouse Gas Adsorption. *Surf. Interfaces* **2025**, *60*, 105988. [CrossRef]
16. Xu, H.; Cui, X.; Qiu, X.; Zeng, W.; Zhou, Q. High-Performance NO_2 Gas Sensors Based on SnS_2/MoS_2@c-MOF Heterojunctions Gas-Sensitive Materials with Different Ratios in Agricultural Greenhouses. *Mater. Today Chem.* **2025**, *49*, 103024. [CrossRef]

17. Yilmaz, O.E.; Yilmaz, A.C. Green-Fabricated Enzyme-Functionalized Chitosan/Cu-BTC Nanofibers for Ultralow-Level, Room-Temperature CO Detection with Enhanced Selectivity and Stability. *Talanta* **2026**, *296*, 128509. [CrossRef] [PubMed]
18. Arkoti, N.K.; Pal, K. Improved Selectivity of Borophene Sensor towards NO_2 Gas with PEI-ZIF-8 Overlayer. *Sens. Actuators B Chem.* **2024**, *401*, 135033. [CrossRef]
19. Aal, S.A.; Soliman, K.A. Enhanced Toxic Gas Detection of CO and NCCl Using Cu and Ni Anchored B-Doped C_9N_4 Nanosheets: A Comprehensive DFT-3D Study. *Diam. Relat. Mater.* **2025**, *151*, 111857. [CrossRef]
20. An, Q.; Li, J.; Peng, J.; Hu, L. DFT Study of Small Gas Molecules (C_2H_2, CH_4, CO and H_2) Adsorbed on Au, Ag-Doped ZnO Monolayer. *Chem. Phys. Lett.* **2025**, *869*, 142043. [CrossRef]
21. Ayesh, A.I. H_2S and SO_2 Adsorption on Cu Doped $MoSe_2$: DFT Investigation. *Phys. Lett. A* **2022**, *422*, 127798. [CrossRef]
22. Bonyani, M.; Mojtaba Zebarjad, S.; Kanani, M.; Moaddeli, M.; Kim, H.W.; Kim, S.S. Au-Decorated ZnO Nanowires for the Detection of NO_2 Gas: A DFT Study. *Appl. Surf. Sci.* **2024**, *657*, 159773. [CrossRef]
23. Batoo, K.M.; Alalaq, I.S.; Mm, R.; Mishra, A.; Sharma, S.; Prasad, G.V.S.; Ijaz, M.F.; Alsaadi, S.B.; Mtasher, A.A.; Seed, F.F. A Novel MoS_2/Pd_5 Nanocluster Heterojunction System with Improved Surface Reactivity for Efficient Gas Sensing: A DFT Study. *Surf. Sci.* **2025**, *752*, 122648. [CrossRef]
24. Thangamani, G.J.; Pasha, S.K.K. Titanium Dioxide (TiO_2) Nanoparticles Reinforced Polyvinyl Formal (PVF) Nanocomposites as Chemiresistive Gas Sensor for Sulfur Dioxide (SO_2) Monitoring. *Chemosphere* **2021**, *275*, 129960. [CrossRef] [PubMed]
25. Cid, B.J.; Santana, J.E.; Arellano, L.G.; Miranda, A.; Pérez-Figueroa, S.E.; Iturrios, M.I.; Pérez, L.A.; Cruz-Irisson, M. Metal-decorated siligene as work function type sensor for NH_3 detection: A DFT approach. *Appl. Surf. Sci.* **2023**, *610*, 155541. [CrossRef]
26. Li, X.; Wang, X.; Sun, Z.; Li, F.; Fu, Y.; Zhao, K.; Zhao, G.; Zhu, C.; Xu, X. Surface Free Radicals Activated CoP/MoS_2 Sensors through Electrocatalytic Water Splitting for Enhanced NO_2 Sensing at Room Temperatures. *Chem. Eng. J.* **2024**, *495*, 153381. [CrossRef]
27. Sun, Y.; Zhang, D.; Tang, M.; Liu, W.; Liu, Y.; Wang, J.; Xi, G.; Xiong, H.; Zhang, L. Trimethylamine Gas Sensor Based on Bimetallic Ag/Cu@$CuFe_2O_4$: Experiment and DFT Calculation. *J. Alloys Compd.* **2025**, *1010*, 177662. [CrossRef]
28. Suleiman, N.; Apalangya, V.; Kan-Dapaah, K.; Mensah, B.; Elloh, V.W.; Yaya, A.; Abavare, E.K.K. Adsorption of CO and CO_2 Interaction with (7,0) AlN Nanotubes to Enhance Sensing Capabilities: A DFT Approach. *J. Phys. Chem. Solids* **2025**, *199*, 112537. [CrossRef]
29. Zhang, D.; Zhu, W.; Li, H.; Lin, L.; Xie, K.; Wang, P.; Zhang, Z. The Adsorption and Gas-Sensing Properties of Transition Metal (Ag and Au) Modified CrS_2 Monolayer: A DFT Study. *FlatChem* **2024**, *48*, 100780. [CrossRef]
30. Bo, Y.; Zhang, Q.; Yang, X.; Wang, B.; Shen, Y. Detection of Harmful Gases (NO, NO_2) by GaN@MoSSe Heterostructures Embedded with Transition Metal (Cu, Fe and Mn) Atoms: A DFT Study. *Surf. Interfaces* **2024**, *54*, 105151. [CrossRef]
31. Cai, H.; Luo, H.; Hu, F.; Wang, J.; Zhou, J.; An, D. High-Response n-Butanol Gas Sensor Based on Quasi-Zn-MOFs with Tunable Surface Oxygen Vacancies. *J. Alloys Compd.* **2025**, *1010*, 177274. [CrossRef]
32. Zhang, H.; Huang, Z.; Jiang, J.; Zeng, W.; Zhou, Q. DFT Study of Cun (n = 1–3) Cluster-Modified WSe_2 Monolayers for the Detection of SF_6 Decomposition Gases (H_2S, SO_2, SOF_2 and SO_2F_2). *Surf. Interfaces* **2024**, *52*, 104904. [CrossRef]
33. Zhang, H.; Jiang, J.; Zhou, W.; Zhou, Q. Investigation of nTiO_2-WTe_2 (n = 1–3) Nanocluster Sensors for the Detection of Toxic Gases H_2S, NH_3, and NO_2 in Agricultural Greenhouses: A DFT Study. *J. Environ. Chem. Eng.* **2025**, *13*, 117879. [CrossRef]
34. Wang, J.; Zhong, X.; Shen, Y.; Li, S.; Qiu, G.; Wang, P.; Tao, L. MgTe for Efficient Adsorption of Lithium-Ion Battery Fault Gases (H_2, CO, and CO_2) and Failure Risk Index Calculation: A DFT Computational Study. *Surf. Interfaces* **2024**, *53*, 104995. [CrossRef]

Disclaimer/Publisher's Note: The statements, opinions and data contained in all publications are solely those of the individual author(s) and contributor(s) and not of MDPI and/or the editor(s). MDPI and/or the editor(s) disclaim responsibility for any injury to people or property resulting from any ideas, methods, instructions or products referred to in the content.